Climate Dynamics (2026) 64:40
https://doi.org/10.1007/s00382-025-07986-0

Integrating an CNOP analysis into a deep learning model to identify optimal initial errors for 2020–2022 La Niña prediction

Lingjiang Tao[1,2] · Rong-Hua Zhang[1,2] · Wansuo Duan[3] · Lu Zhou[1,2] · Tiaoye Li[2]

Received: 31 May 2025 / Accepted: 6 November 2025

Abstract

Leveraging the Conditional Nonlinear Optimal Perturbation (CNOP) approach, this study introduces an innovative adjoint-free methodology to discern optimal initial errors (OIEs) that influence the prediction of the 2020–2022 multi-year La Niña events in a data-driven transformer model. Both being characterized by three-dimensional (3D) structures and capable of inducing maximum error, two distinct types of OIEs are identified: one with positive OIE in the upper eastern Pacific (POIE) and another with a similar structure but negative OIE (NOIE). Dynamically, these OIEs trigger a strong Bjerknes feedback mechanism, thus leading to rapid error growth. Conducting target observing experiments intensified in these regions with large values of OIEs can further improve the 2020–2022 La Niña events by reducing the prediction errors to 80% at most. From predictability point of view, compared to 2020 and 2022 La Niña, the prediction of the 2021 La Niña is more sensitive to initial conditions, underscoring the insight that the predictability of the consecutive La Niña events is of complexity in nature. The innovative integration of the CNOP approach into a deep learning model offers a new framework for improving ENSO prediction and predictability.

Plain language summary

In line with dynamical models, data-driven models also suffer from the influence of initial errors when predicting ENSO events. How errors in initial input fields (i.e., initial conditions) can affect predictions in a data-driven model is unclear. In this study, we present an innovative framework by integrating an adjoint-free Conditional Nonlinear Optimal Perturbation (CNOP) method with a data-driven model (the 3D-Geoformer) to investigate the sensitivity to initial condition during the prediction of the 2020–2022 La Niña events. Two types of initial temperature errors that can cause the largest errors in predicting the La Niña events: one features positive values (POIE) in the eastern tropical Pacific, while the other is similar but with negative values (NOIE). These errors are amplified due to the air-sea coupling, generating the "butterfly effect". The 2021 La Niña prediction is particularly sensitive to initial errors, making it harder to predict accurately compared to the 2020 and 2022 events. Furthermore, the prediction errors resulting from POIE are larger than those from NOIE. By breaking down the processes that cause these errors to grow, the differences in sensitivity are attributed to the triggered Bjerknes feedback. In summary, this innovative approach (adjoint-free CNOP) provides a novel perspective on predictability studies, significantly advancing our ability to analyze and mitigate prediction errors in complex climate systems. This study not only identifies the 3D structure of OIEs and their impacts on La Niña predictions, but also introduces an innovative 3D CNOP analysis framework within a data-driven model context, offering a new perspective on ENSO-related predictability studies.

✉ Rong-Hua Zhang
rzhang@nuist.edu.cn

✉ Wansuo Duan
duanws@lasg.iap.ac.cn

[1] State Key Laboratory of Climate System Prediction and Risk Management, Nanjing 210044, China

[2] School of Marine Sciences, Nanjing University of Information Science and Technology, Nanjing 210044, China

[3] State Key Laboratory of Earth System Numerical Modeling and Application, Institute of Atmospheric Physics, Chinese Academy of Sciences, Beijing 100029, China

Published online: 06 January 2026

Public summary

- The Conditional Nonlinear Optimal Perturbation (CNOP) is successfully integrated with a data-driven transformer model to identify the optimal initial errors for ENSO.
- The prediction of multi-year La Niña event during 2020–22 exhibit varying sensitivities to the initial condition which can be explained by the differences in the Bjerknes feedback.
- Improving the initial condition in the CNOP-identified area can further reduce the prediction errors by up to 80% during the 2020–22 La Niña conditions.

1 Introduction

El Niño-Southern Oscillation (ENSO) represents one of the most powerful interannual signals in the climate system (Philander 1983). During ENSO cycles, anomalous warming (El Niño) and cooling (La Niña) alternately occur in the central-eastern equatorial Pacific, which trigger large-scale anomalies in the atmosphere and influence various regions globally through the atmospheric bridge (Alexander et al. 2002), thus having profound impacts on the environment and society (Yeh et al. 2009). Therefore, the timely accurate prediction of ENSO events and enhancing the understanding of ENSO predictability are major scientific hotspot issues that are closely watched by meteorologists and the public.

Over the past few decades, historical progress has been achieved in the simulation and prediction of ENSO. Particularly, the rapid development of numerical models built under the framework of dynamical equations (so-called dynamical models) has greatly enriched the studies of ENSO predictability (Duan and Mu 2018; Liu et al. 2023, 2022; Lou et al. 2023; Tan et al. 2020; Tang et al. 2018; Zhang et al. 2020; Gao et al. 2022). Research consistently shows that the prediction skill of models for ENSO is highly dependent on the accuracy of the initial condition, and an effective initialization approach can substantially improve both the precision and timeliness of ENSO predictions (Chen et al. 1997; Rao et al. 2023; Zheng et al. 2023). Furthermore, induced by the unstable state of the air–sea coupling in spring, the ENSO prediction errors caused by initial errors typically experience rapid growth during spring, thereby significantly constraining the prediction skill of ENSO. Such a problem with prediction error growth caused by initial errors is known as the first predictability problem. Investigating the first predictability problem is not only a crucial aspect in comprehending the predictability of ENSO but also helpful in theoretically guiding the improvement in ENSO predictions.

The conditional nonlinear optimal perturbation (CNOP) approach, proposed by Mu et al. (2003), is an important method for studying the first predictability problem. Based on an intermediate coupled model and CNOP approach, Yu et al. (2009) identified a dipole pattern of the initial errors in sea surface temperature (SST) along the equator has the worst effect on the El Niño prediction. Therefore, intensifying observations in these key ocean regions is needed to avoid the occurrence of such type of initial errors, acting to mitigate the initial error-induced prediction error, thus effectively improving ENSO predictions (Duan et al. 2018). Subsequently, more complicated models equipped with the CNOP approach have been used to investigate the sensitivity of ENSO predictions to initial conditions (Duan and Hu 2016; Qi et al. 2021), further identifying the initial errors in extratropical Pacific regions that most significantly impact ENSO predictions (Hou et al. 2019). The former studies on ENSO predictability undoubtedly provide scientific theoretical guidance for target observations of ENSO. Since ENSO is becoming more diverse and complex under the context of global warming (Geng et al. 2023; Timmermann et al. 2018), the problems with current dynamical models in simulating ENSO are increasingly evident (Feng et al. 2020; Freund et al. 2020; Tao et al. 2020, 2022). This has directly resulted in a collective decline in ENSO forecasting skills among various operational units (Jin et al. 2008; Zhang et al. 2022).

More recently, ENSO models developed based on the artificial intelligence (AI) technology have rapidly risen after the pioneering work of Ham et al. (2019), demonstrating remarkable ENSO forecasting skills (e.g., Ham et al. 2021; Ibebuchi and Richman 2024; Mu et al. 2021, 2022; Zhou and Zhang 2022). These data-driven AI models not only have a unique advantage in ENSO predictions but also contribute to deepening our understanding of ENSO predictability and dynamics (Gao et al. 2023; Zhou and Zhang 2024; Li et al. 2024; Wang et al. 2024; Zhang et al. 2024b). For instance, using the data-driven model, Gao et al. (2023) investigated the impact of the negative subsurface sea temperature anomaly during 2021 on the simulation and prediction of the following La Niña event by modifying the feature of the initial conditions (i.e., input fields). Their results preliminarily indicate that the first predictability problem also exists in AI models. Given this, it is of interest to know how predictable ENSO is for AI models, and what kind of initial errors would have the greatest impact on the prediction.

However, the sensitivities of ENSO predictions to initial conditions have not been systematically explored in data-driven models (Qin et al. 2024). Most previous studies typically alter initial conditions and then examine their effects

in a subjective and manual manner (e.g., Gao et al. 2023; Wang et al. 2024). In this study, we pioneer the integration of the CNOP approach into a data-driven transformer model to investigate optimal initial errors (OIEs) that exert the most significant influence on ENSO predictions. Using the three consecutive La Niña events from 2020 to 2022 as a case study, we systematically examine their effects on the predictability of La Niña events. Our focus on these events is driven by two key motivations: first, AI models have demonstrated superior performance over dynamic models in simulating and predicting these exceptional ENSO events; second, it is particularly interesting to explore the differing sensitivities to initial conditions across the three La Niña events (Gao et al. 2023; Zhang et al. 2024a, b; Dong et al. 2025). This innovative research will not only highlight the critical role of initial conditions in AI-based predictions, but also provide theoretical support and practical insights for the future improvement of data-driven ENSO models.

2 Model and method

2.1 A data-driven transformer-based model

Taking the advantage in dealing with multi-variable and three-dimensional air-sea coupling, the 3D-Geoformer developed by Zhou and Zhang (2023) is adopted to investigate the optimal initial errors in this study. The overall architecture of 3D-Geoformer consists of four core modules: the data preprocessing module, the encoder module, the decoder module, and the output module. The data preprocessing module receives as input continuous 12 months of sea surface meridional and zonal wind stress, as well as 7 layers of sea temperature fields within the upper 150 m (totaling 9 layers for the input air-sea data). The input fields only cover the tropical Pacific (92°E-330°E, 20°S-20°N). Within this module, the input data undergoes spatial field segmentation, patch encoding (embedding), and the embedding of spatiotemporal positional information. The processed data is then passed to the encoder module. The encoder and decoder modules are internally constructed with multiple layers of transformer blocks. Within the transformer blocks, a crucial component for model prediction is the spatiotemporal self-attention module, which is built entirely on self-attention mechanisms without any convolution or recurrence operations. Notably, differed from the end-to-end prediction methods commonly used in most AI prediction models, a rolling prediction scheme is equipped in the 3D-Geoformer. This approach effectively realizes monthly coupling between oceanic and atmospheric variables, thereby mimicking the Bjerknes feedback process within the deep learning framework, enhancing the interpretability of the model's prediction process.

With inherent advantages in analyzing spatiotemporal information within multivariable fields, the 3D-Geoformer boasts greater flexibility and exploratory potential than previous AI models. For example, by altering the time span of the input variable field, one can explore the optimal precursory period of ENSO. Also, by artificially modifying the three-dimensional structure of the input field (e.g., subsurface sea temperature), important oceanic processes leading to ENSO can be revealed (e.g., Gao et al. 2023; Zhang et al. 2024a). Furthermore, in terms of prediction, the 3D-Geoformer also demonstrates impressive performance. Particularly in handling and predicting complex ENSO events, its advantages are more pronounced. For example, the 3D-Geoformer can capture the three-dimensional evolution of sea temperature over a year in advance for the extremely rare triple-year-long La Niña event from 2020–2022. Even when forecasting initiated in the spring, the model could still accurately predict the evolution trajectory of sea surface temperature anomalies in the central-eastern Pacific and the intensities of the three La Niña events (Fig. 1). Then, the interesting thing is what outcomes the 3D-Geoformer would predict if the initial input field is perturbed. By doing so, we can explore the sensitivity of the three La Niña predictions in the data-driven model to the initial field and identify the initial error that exerts the largest prediction errors. Such method involved is the CNOP.

2.2 CNOP approach

The CNOP approach firstly proposed by Mu et al. (2003) is used to search for a constrained initial error that is capable of inducing the maximal evolution of prediction errors in a numerical model. However, due to the reliance on adjoint models to compute gradients during the calculation process, CNOP is challenging to implement in large models or those lacking adjoint modules. Fortunately, several methods have been developed in recent years to solve CNOP without requiring adjoint models, one of which involves optimization using large-sample data (Duan and Hu 2016). Building on this foundation, this study will further optimize the method to obtain a CNOP solution with higher precision, following these steps:

2.2.1 a. Generation of large initial perturbation samples

To ensure that the perturbation samples are ergodic and physically meaningful, we utilized data from 23 models in CMIP6 (each spanning 165 years) and data from GODAS from 1980 to 2022 (covering 43 years). As previous studies (Duan and Hu 2016), monthly average ocean temperature data from

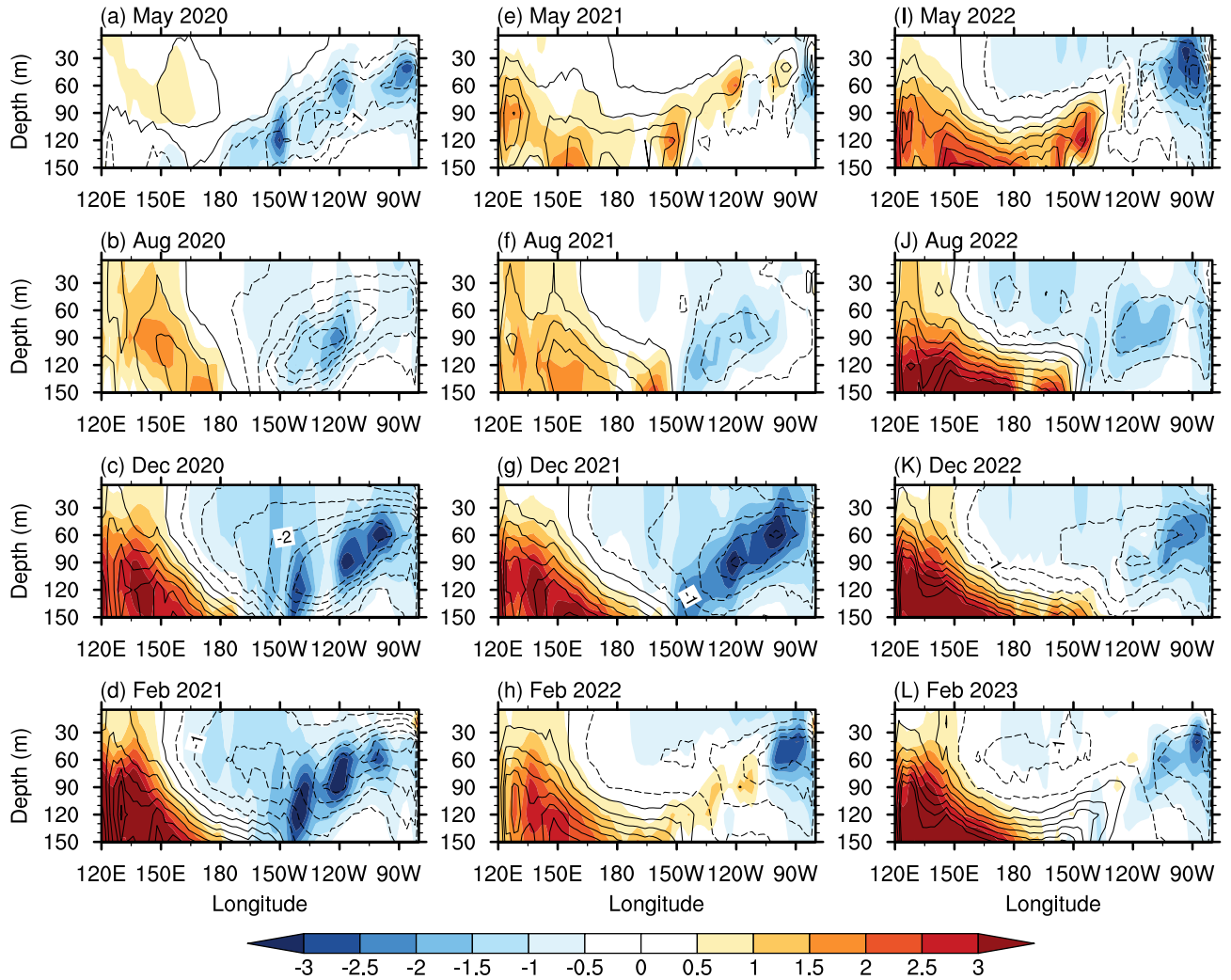

Fig. 1 Zonal-depth sections of the observed (shaded) and predicted (contoured) ocean temperature anomalies along the equator for the 2020–2022 La Niña events. The predictions are made by the 3D-Geoformer starting each year in May. That is, the data used to drive the 3D-Geoformer forecasts are the air-sea fields from the 12 months prior to the current May (excluding May itself). The contour interval is 0.5 °C

January, April, July, and October are selected as initial perturbations. Additionally, 100 groups of random errors were generated. To maintain sample unbiasedness, the opposite phases of each are taken as new perturbation samples. By this way, we can generate a larger sample of initial perturbations with ergodicity and dynamic characteristics. Consequently, the total number of perturbation samples generated is $((165 \times 23 + 43) \times 4 + 100) \times 2 = 30904$ (Table 1).

2.2.2 b. Constraining the perturbations

The initial perturbation samples cannot be directly added to the initial field and require preprocessing. Given that we are only considering the impact of initial perturbations in ocean temperature in the tropical Pacific, the perturbations in the tropical Pacific region (20°N–20°S, 120°E–70°W) are extracted. Furthermore, these perturbation samples are normalized, constraining, or amplifying the total perturbation energy ($\sum_{i,j,k} (T_{i,j,k}\prime)^2$) to 10^8 °C^2, equivalent to a root mean square error (RMSE) of 0.5 °C.

c. Perturbated predictions:

The constrained perturbation samples are added only to the input field in April. The subsequent ocean–atmosphere conditions are predicted using the 3D-Geoformer. For each La Niña event, we can generate 30,904 prediction samples.

d. Ensemble iterative optimization:

Compared to the control prediction (Fig. 1), adding initial perturbations would cause the results to deviate from the control prediction. To quantify the forecast errors induced by perturbations, an objective function is defined:

Table 1 Details of the large initial perturbation samples used to the ensemble-based CNOP analysis

No	Sources of perturbations	Period	Total number of perturbation samples
1	ACCESS-CM2	January, April, July, and October during the period from 1850 to 2014	With the opposite ones, the total number of perturbation samples is $((165 \times 23 + 43) \times 4 + 100) \times 2 = 3090$
2	ACCESS-ESM1-5		
3	AWI-CM-1–1-MR		
4	CAMS-CSM1-0		
5	CanESM5-CanOE		
6	CESM2		
7	CESM2-WACCM		
8	CESM2-WACCM-FV2		
9	E3SM-1–0		
10	E3SM-1–1		
11	FGOALS-f3-L		
12	FGOALS-g3		
13	FIO-ESM-2–0		
14	GFDL-CM4		
15	GFDL-ESM4		
16	HadGEM3-GC31-LL		
17	IPSL-CM6A-LR		
18	MIROC6		
19	MIROC-ES2L		
20	MRI-ESM2-0		
21	NESM3		
22	NorESM2-MM		
23	SAM0-UNICON		
24	Reanalysis data: GODAS	January, April, July, and October during 1980–2020	
25	Random errors	100 samples	

$J = \sqrt{\frac{1}{N}\sum_{i,j}\left(SST^{p}_{i,j} - SST^{ctl}_{i,j}\right)^2}$, where $SST^{p}_{i,j}$ and $SST^{ctl}_{i,j}$ is the predicted SST anomaly in model grid (i, j) in Niño3.4 in perturbation and control prediction experiments, respectively. Based on the values of the objective function and the direction of error evolution, the top 50 groups of perturbation samples that lead to the largest positive and negative error developments are selected. These are then ensemble averaged and re-constrained to produce new perturbation samples. These new samples are then compared with the original 50 samples, and iterative replacements are conducted. This process continues until the error growth induced by the 50 disturbance samples shows negligible differences. The ensemble average of these 50 groups represents the optimal initial error we seek. For instance, in the case of the 2020 La Niña event, we initially select the top 50 groups that cause the maximum development of forecast errors and result in positive Niño3.4 errors, denoted as $(T_1, T_2, T_3, \ldots, T_{50})$. The ensemble average of these 50 perturbation samples is re-constrained to obtain a new perturbation sample, denoted as T_{k1}. Based on the objective function, new top 50 groups of maximum error samples are selected, incorporating T_{k1} and excluding one of the previous samples, e.g., $(T_1, T_2, T_3, \ldots T_{k1} \ldots, T_{49})$. This iterative process continues until convergence, yielding the final T_{kn}, which is the optimal initial perturbation causing the most severe underprediction in the 2020 La Niña event.

The innovative use of ensemble iterative optimization in this study effectively circumvents the challenges associated with solving the adjoint in dynamical and data-driven models. By leveraging large-sample calculations, this approach pioneers a practical and efficient method to obtain the CNOP without relying on traditional adjoint-based techniques.

3 Results

3.1 Optimal initial errors

From the large ensemble perturbation prediction experiment, although the perturbations we applied are small and only superimposed on the input fields in April, almost all perturbed predictions gradually deviated from the control forecasts over the integration time. In other words, the prediction using the data-driven model is indeed dependent on the accuracy of the initial conditions. This also indirectly confirms the advantage of the 3D-geoformer in displaying the "butterfly effect" feature, attributed to its capability of identifying nonlinear relationships between multiple variables through large ocean–atmosphere data (Zhang et al.

2024b). Statistical analysis reveals that samples with larger prediction error growth often exhibit similar spatial structures. Through continuous iteration, we identified the optimal initial errors (OIEs) that can induce the largest error growth for the predictions of these three La Niña events. It is found that the distribution characteristics of the OIEs are nearly consistent for three La Niña predictions. Each La Niña prediction has two similar patterns of CNOP solutions but with opposite phases (see Fig. 2): one type is of positive value mainly (hereafter termed POIE), and the other is of negative value (hereafter termed NOIE). OIEs are mainly distributed in the upper 150 m of the tropical central and eastern Pacific Ocean. Vertically, the maximum error is located around 110°W, at a depth of about 50 m. As to the surface horizontal distribution, the error signals of OIEs are mainly concentrated in the equatorial eastern Pacific and the tropical southeastern Pacific.

Dynamically, the distribution structure of OIEs is nearly identical to the Bjerknes mode proposed by Yu and Fang (2018). Specifically, when large-scale sea temperature anomalies appear in the central and eastern Pacific, coupled with surface wind anomalies, it will form a strong positive feedback mechanism and further amplify the SST anomalies in the central and eastern Pacific. It is precisely the Bjerknes mode-like presented by OIEs that allows initial errors to grow rapidly under a strong positive feedback mechanism. One can easily see that the near-opposite phases of POIE and NOIE lead to contrasting prediction error evolution trajectories: the prediction error growth resulting from POIE is akin to the development of El Niño (Fig. 3a), which hampers the ability of the model to predict the cold event. Conversely, the prediction error growth associated with NOIE resembles the development of La Niña (Fig. 3d), causing the model to predict a La Niña event that is stronger than what actually materializes.

3.2 Sensitivity to the initial errors

We will now explore how POIE and NOIE affect these three La Niña predictions to evaluate the sensitivity of the predictions for the three La Niña events to the initial conditions. In this section, we first use the forecast error of the Niño34 index to quantify the effect of OIEs on the prediction of La Niña intensity (see Fig. 3a and c). One common feature is that as the prediction time increases, the prediction error in the Niño3.4 index progressively grows, reaching its maximum at the end of year and then gradually decreasing. However, while the most unstable modes of initial errors (i.e., OIEs) among the three La Niña predictions are similar, error growth rates induced by OIEs vary. Notably, when POIE is added to the initial conditions, its impact on the 2021 La Niña prediction is greater than that on the predictions of other La Niña events, with error in Niño3.4 index reaching up to 1.7 °C. Another distinction is that the prediction error induced by POIE is larger than that by NOIE. This suggests that the initial errors are more likely to produce positive SST errors in the central-eastern Pacific, resulting in the underestimation of the La Niña event.

It is essential to highlight that La Niña is not merely a localized sea surface cooling event confined to the Niño3.4 region, but rather a comprehensive cooling phenomenon extending throughout the upper ocean. Thus, the prediction error in the Niño3.4 index cannot fully indicate the sensitivity of La Niña prediction to the initial conditions. To this end, the RMSEs of SST in the Niño3.4 region and sea temperatures in the upper ocean of the tropical Pacific are also calculated. The RMSEs are mathematically defined as $RMSE = \sqrt{\frac{1}{N}\sum_{i,j,k}\left(T^{p}_{i,j,k} - T^{o}_{i,j,k}\right)^{2}}$, where $T^{p}_{i,j,k}$ and $T^{o}_{i,j,k}$ are the predicted SST anomalies in the model grid (i,j,k) from perturbed and original prediction experiments. As can be observed, the square of RMSEs in the upper ocean can characterize the evolution of the initial error energy.

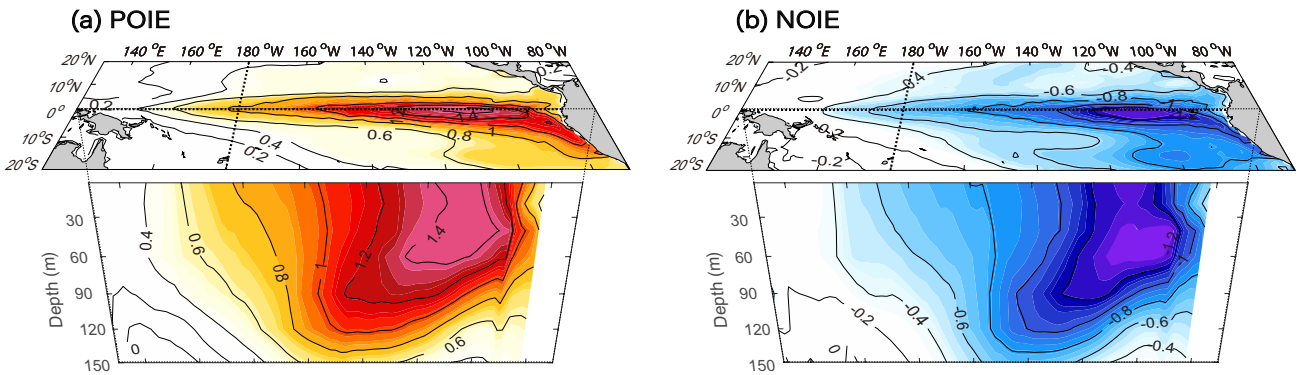

Fig. 2 Three-dimensional spatial distributions of optimal initial errors that have the worst impact on La Niña prediction. One optimal initial error is primarily positive **a**, denoted as POIE; the other is primarily negative **b**, denoted as NOIE

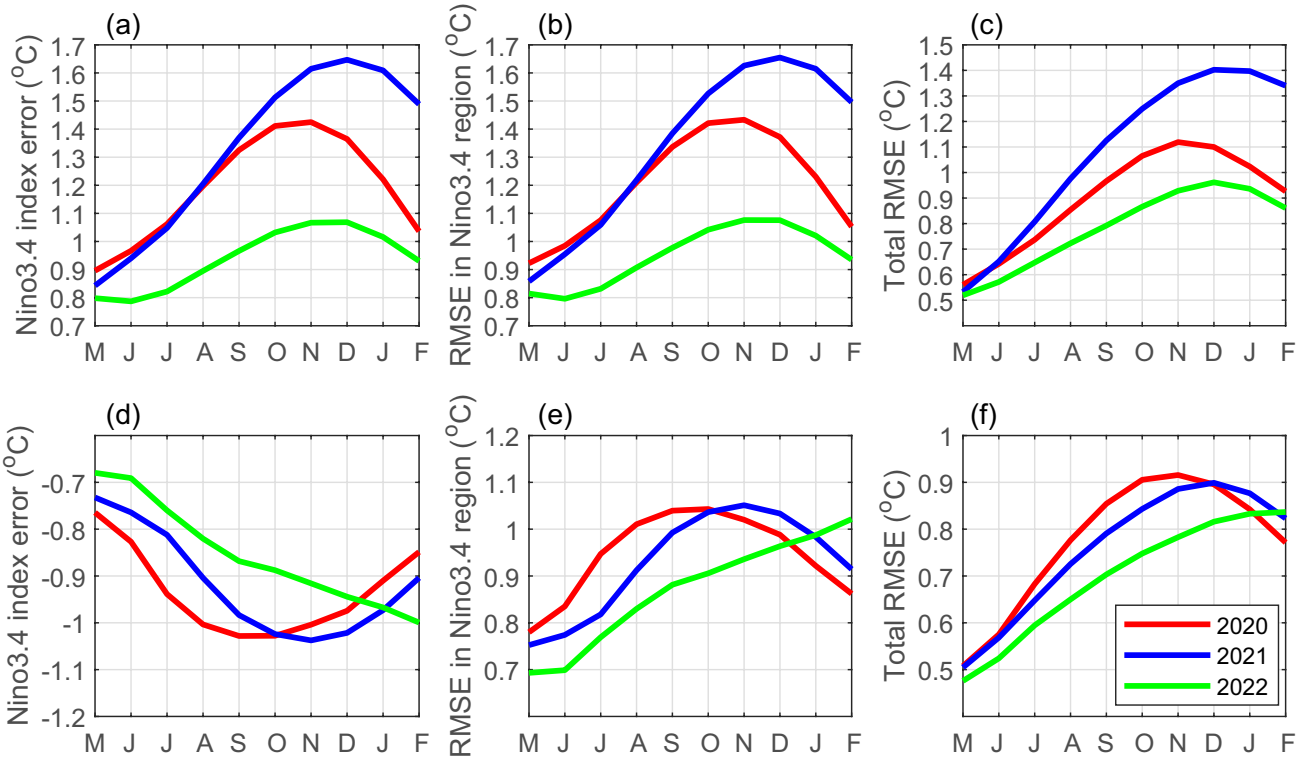

Fig. 3 **a**–**c** POIE-induced and **d**–**f** NOIE-induced prediction errors for three La Niña predictions. **a** and **d** present the prediction error in the Niño3.4 index. **b** and **e** show the root mean square error (RMSE) of SST anomalies in the Niño3.4 region, and RMSEs in **c** and **f** are calculated among the whole tropical Pacific resolved by the 3D-Geoformer

Upon integrating the characteristics of the three categories of error evolution (Fig. 3), it becomes evident that the derived OIEs exert a profound influence not only on the temperature prediction in the Niño3.4 region but also on those in the upper layers of the tropical Pacific Ocean. In certain instances, the rate of error growth in the subsurface exceeds that of surface error growth. As shown in Fig. 3c, the RMSE of temperature caused by POIE across the entire tropical Pacific can exceed 1.4 °C. Viewed from the perspective of energy growth, the initial energy of perturbation develops rapidly, increasing by at least 5–6 times compared with the initial error. This fully demonstrates the catastrophic impact of the "butterfly effect" on predictions.

Note that POIE and NOIE represent the optimal solutions for positive error and negative error growth, respectively. The induced predictions also represent the maximum and minimum SST anomalies in the prediction with the model. The greater the difference between the two predictions, the more sensitive it is to the initial condition. According to Fig. 3a and d, we can conclude that the initial perturbation can induce a larger spread for the 2021 La Niña prediction than the 2020 and 2022 La Niña predictions. It is implied that the 2021 La Niña prediction is more sensitive to the initial condition. What's more, OIEs also tend to generate larger error energy for predicting the 2021 La Niña event. Based on the analyses of RMSEs in Fig. 3, it is concluded that the 2021 La Niña prediction is much more reliant on initial conditions compared to the 2020 and 2022 La Niña predictions. That is, Fig. 3 implies that the 2021 La Niña has the lowest predictability.

Additionally, comparing the error growth caused by POIE and NOIE, it is not difficult to find that the former produces stronger error energy in both the Niño3.4 region and the entire tropical Pacific. This suggests that La Niña predictions are more sensitive to positive initial errors in sea temperature. In other words, given the presence of initial condition errors, the model tends to yield La Niña events that are weaker in intensity compared to the observed events.

3.3 Factors contributing to sensitivity differences

The aforementioned findings indicate that, firstly, the predictability of the 2021 La Niña is the poorest, and initial errors are more prone to result in substantial prediction discrepancies. Secondly, for those three La Niña events, the prediction errors induced by the POIE is significantly larger than that caused by the NOIE. In other words, the sensitivity of La Niña prediction to POIE was higher than to NOIE. The question naturally is raised: what accounts for this difference in sensitivity?

From the perspective of error evolution, the error evolution trajectory bears resemblance to the development of an El Niño or La Niña. Not only does the ocean temperature error undergo continuous development, but the wind stress error also develops successively (Fig. 4). Undoubtedly, this is the outcome of the nonlinear interaction between the ocean and atmosphere, which allows the prediction errors of various variables to develop rapidly under the Bjerknes positive feedback mechanism. Take the 2020 La Niña perdition as example, when the POIE (NOIE) is added in the initial condition, the tropical Pacific is featured by the deepened (shallowed) thermocline and positive (negative) SST anomaly in the eastern tropical Pacific. The perturbed ocean will couple with west (east) wind anomaly over the central tropical Pacific to make the air-sea unstable. That is, from the perspective of error growth, OIEs also tend to trigger a strong positive feedback process that causes the initial error to continually develop.

The differences in sensitivity are manifested in the varying magnitudes of prediction error, implying that the Bjerknes positive feedback mechanisms they trigger diverge in certain aspects. Hence, to uncover the causes of the predictability differences, the Bjerknes positive feedback process is decomposed into the SST-Wind feedback, Wind-Heat Content (HC) feedback, and HC-SST feedback (Planton et al. 2021). The SST-Wind feedback represents the response of the wind anomaly over the central and western tropical Pacific to the SST anomaly in the eastern tropical Pacific. The Wind-HC feedback represents the process wherein the forcing of the surface wind on the ocean results in thermocline anomaly (i.e., HC) in the eastern Tropical Pacific. The HC-SST feedback denotes the effect of subsurface temperature anomaly on the SST in the eastern tropical Pacific. Hence, according to the error evolutions in Fig. 4, the error in HC in the eastern tropical Pacific (10° S–10° N, 170° W–120° W) regressed onto the error in the zonal wind stress over the central and western Tropical Pacific (10° S–10° N, 130° E–150° W) is used to quantify the strength of the SST-Wind feedback, so as the HC-SST and Wind-HC feedbacks. The quantification of the HC-SST and wind-HC feedbacks follows a similar approach.

The strengths of Bjerknes feedback terms are presented in Table 2. It is evident that compared with the 2020 and 2022 La Niña events, OIEs stimulate stronger SST-Wind feedback and HC-SST feedback during the prediction of the 2021 La Niña event, facilitating the rapid development of initial errors. When the Bjerknes feedback processes triggered by POIE and NOIE are contrasted, the former is far higher than the latter in the HC-SST feedback, rendering the positive ocean temperature error in the subsurface layer more likely to influence the surface layer and thereby causing a more significant increase in prediction errors.

4 Implication for target observation

The three-dimensional distributions of OIEs (including POIE and NOIE) in Fig. 2 indicate that the initial temperature errors in the equatorial eastern Pacific and the tropical southeastern Pacific might be the source of the rapid development of prediction errors induced by OIEs. To verify this hypothesis, we retain errors from specific regions of the OIEs and look at how these-induced prediction errors evolve over time. We select three regions with relatively large OIEs: EP, NTP and SETP. EP denotes eastern tropical Pacific (upper 150 m, 5° N–5° S, 170° W–80° W). NTP denotes the north tropical Pacific (upper 40 m, 5° N–20° N, 120° E–70° W). SETP denotes the southeastern tropical Pacific (upper 40 m, 5° S–20°S, 140° W–70° W). Additionally, in the EP region, there are strong errors in the subsurface layer. Therefore, we further divided EP into two parts: the upper 40 m one (EP1) and the below one (EP2). Then, we retain only the initial errors in these regions and add them to the initial conditions. The input data with these partial OIE drive the 3D-Geoformer to yield new predictions. The prediction errors are shown in Fig. 5. By calculating the ratios of these RMSEs to RMSEs caused by OIE, we can observe that the initial errors in the EP1 and SETP most explain the OIEs-induced error growth. This result verifies the hypothesis that the initial errors in the EP1 and SETP are key sources of rapid error growth in La Niña predictions.

Of course, the initial errors in these key regions cannot fully explain the error development induced by OIEs. On the one hand, the error interaction between regions will promote the further development of prediction errors; on the other hand, since only partial initial errors are retained, the energy of these initial errors is much smaller than that of OIEs, especially the error energy in the SETP region. To fairly compare the importance of each region, we amplified these local errors to an energy level comparable to that of OIEs. Then these local errors are added to the initial condition to investigate the error growth they caused in the La Niña prediction (dark blue bars in Fig. 5). It can be found that the error growth caused by the initial errors in the SETP region is the strongest, approaching the error growth caused by OIEs. This means that SETP is the most sensitive area for La Niña prediction.

The former sensitivity experiments also imply that reducing the initial errors in these two regions (EP1 and SETP) may help suppress the growth of errors, thereby improving the prediction skill of La Niña events. To verify this hypothesis, we designed an ideal Observing System Simulation Experiment (OSSE) with the following specific design: First, 1000 sets of observational errors are randomly generated and added to the initial condition in April to serve as the observational fields. These observational fields are then

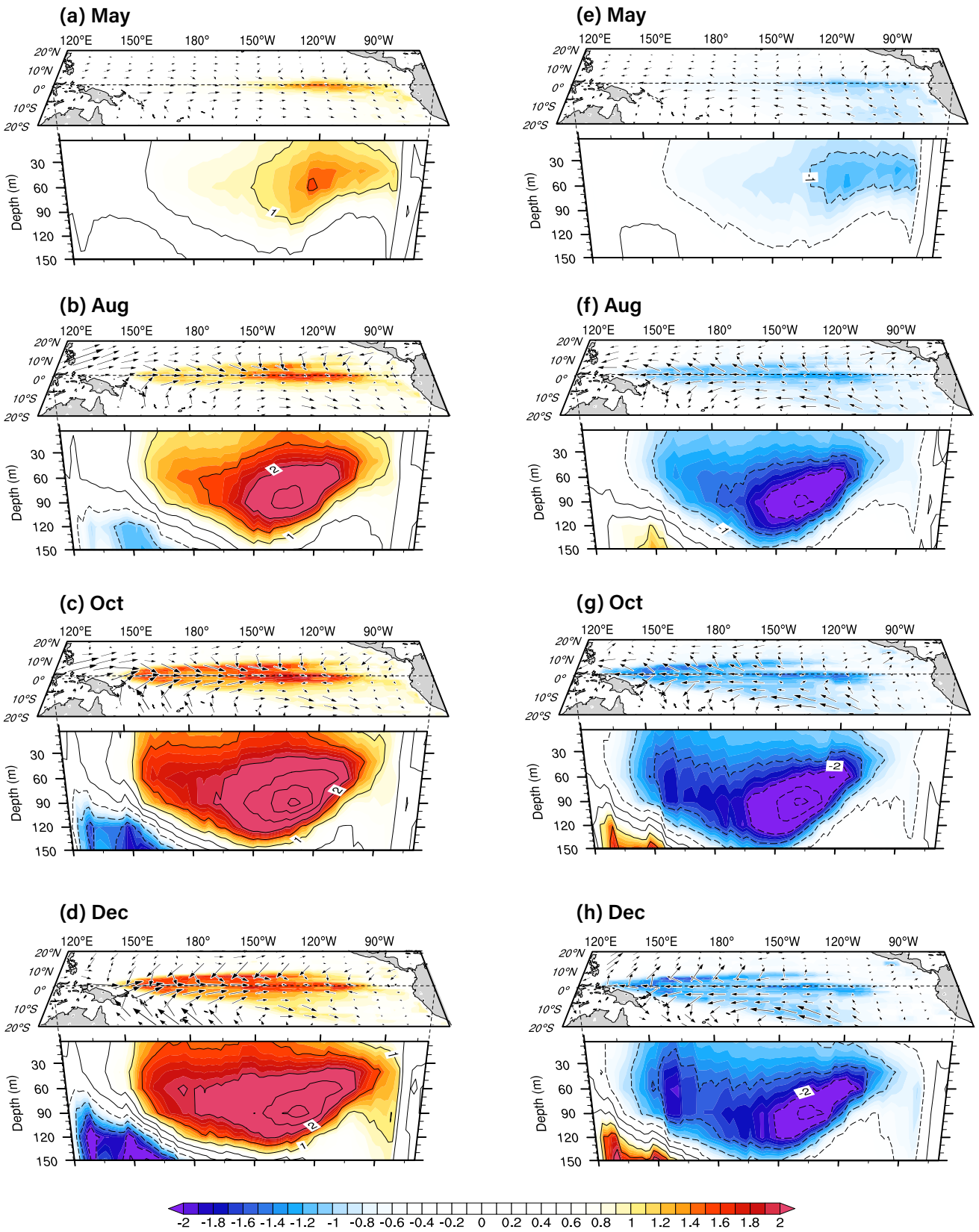

Fig. 4 Spatiotemporal evolutions of the prediction errors in ocean temperature (shaded) and wind stress (vectors) that are induced by the **a**–**d** POIE and **e**–**h** NOIE during the 2020 La Niña prediction. The contour interval is 0.5 °C

Table 2 Three components of Bjerknes feedback terms induced by POIE and NOIE for 2020–2022 La Niña events

		SST-wind feedback ($\times 10^{-2} N/m^2$ °C)	Wind-HC feedback ($\times 10^{-3} m^3$ °C/N)	HC-SST feedback ($\times 10^{-3}$)
La Nina events	2020	0.83±0.06	17.46±1.29	6.66±0.37
	2021	0.98±0.09	12.71±1.07	7.72±0.47
	2022	0.90±0.08	14.57±1.31	7.32±0.35
Phases	POIE	1.07±0.33	9.38±3.04	5.50±0.88
	NOIE	1.25±0.54	9.65±5.53	2.75±0.49

used to re-drive the data-driven model, resulting in 1000 new sets of predictions, denoted as the RE experiment. Subsequently, to simulate the observations in the sensitive regions, we artificially remove the observational errors in the sensitive areas identified by the OIEs to represent the optimized initial conditions after intensified observations. Regarding the locations of the sensitive regions, we design three groups of experiments (see Table 3): an experiment in which only the observational errors in the surface eastern equatorial Pacific (upper 40 m, 5° N–5° S, 170° W–80° W) are removed (denoted as RE_{noEP1}), an experiment in which only the observational errors in the tropical southeastern Pacific (upper 40 m, 5° S–20° S, 140° W–70° W) are removed (denoted as RE_{noSETP}), and an experiment in which the observational errors in both regions are removed simultaneously (denoted as $RE_{noEP1\&SETP}$). Finally, the optimized initial conditions are used to drive the model to obtain the optimized predictions. Through comparative experiments, the effect of "observations" in the sensitive regions on prediction improvement can be analyzed.

Table 3 The description of the ideal observing system simulation experiment

Abbreviation	Description
RE	Predictions with 1000 sets of observational errors
RE_{noEP1}	Target observation predictions in which only the observational errors in the surface eastern equatorial Pacific (upper 40 m, 5° N-5° S, 170° W-80° W) are removed
RE_{noSETP}	Target observation predictions in which only the observational errors in the tropical southeastern Pacific (upper 40 m, 5° S–20° S, 140° W–70° W) are removed
$RE_{noEP1\&SETP}$	Target observation predictions in which the observational errors in both EP1 and SETP regions are removed simultaneously
RE_{RA01}	Random target observation predictions in which the observational errors near the equatorial Pacific (upper 40 m, 6° N–6° S, 120° E–80° W) are removed
RE_{RA02}	Random target observation predictions in which the observational errors in the north tropical Pacific (upper 40 m, 0°–20° N, 150° E–112° W) are removed
RE_{RA03}	Random target observation predictions in which the observational errors in the south tropical Pacific (upper 40 m, 0°–20° S, 180° E–90° W) are removed
RE_{RA04}	Random target observation predictions in which the observational errors in the subsurface Pacific (60–150 m, 6° N–6° S, 120° E–80° W) are removed

Figure 6 displays the changes of the prediction error after "observing" the CNOP identified sensitive regions. As we can see, regardless of which intensified observation

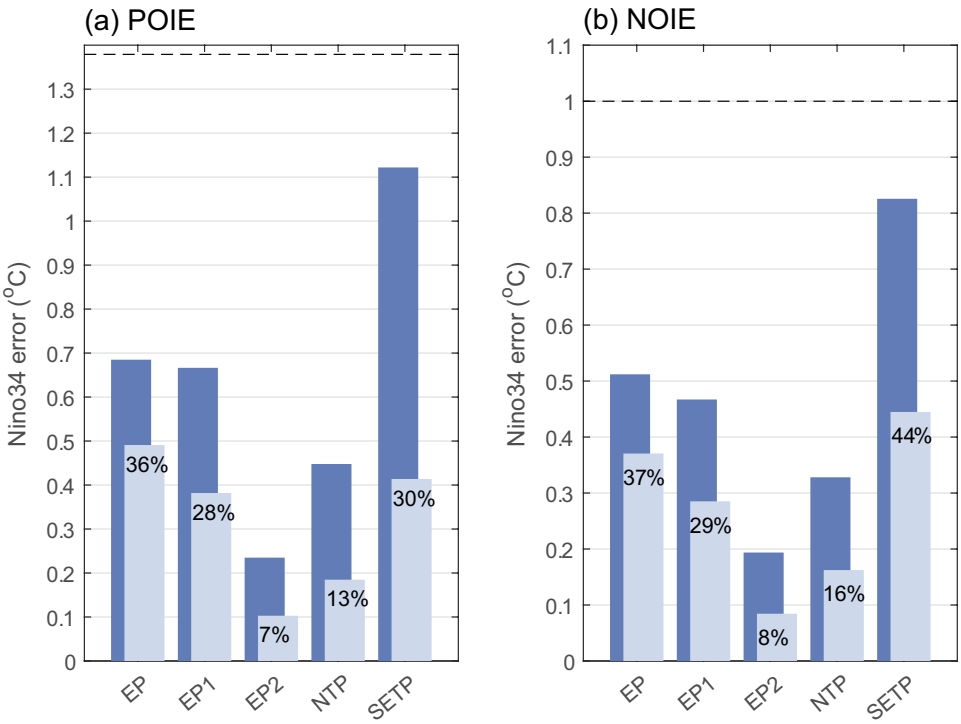

Fig. 5 Contributions of the partial POIE and NOIE to the error growth. The dashed lines in **a** and **b** represent the RMSE of SST in the Niño3.4 region caused by the POIE and NOIE, respectively. The light blue bars indicate RMSEs caused by partial POIE in a specific oceanic region, on which the percentages overlaid represent the ratios of these RMSEs to RMSEs caused by total (**a**) POIE and (**b**) NOIE. The dark blue bars represent RMSEs caused by the amplified initial errors (equivalent in energy to OIEs). EP denotes eastern tropical Pacific (upper 150 m, 5° S–5° N, 170° W–80° W), where EP1 and EP2 are located above and below a depth of 40 m in this region respectively. NTP denotes the north tropical Pacific (upper 40 m, 5° N–20° N, 120° E–70° W). SETP denotes the southeastern tropical Pacific (upper 40 m, 5° S–20° S, 140° W–70° W)

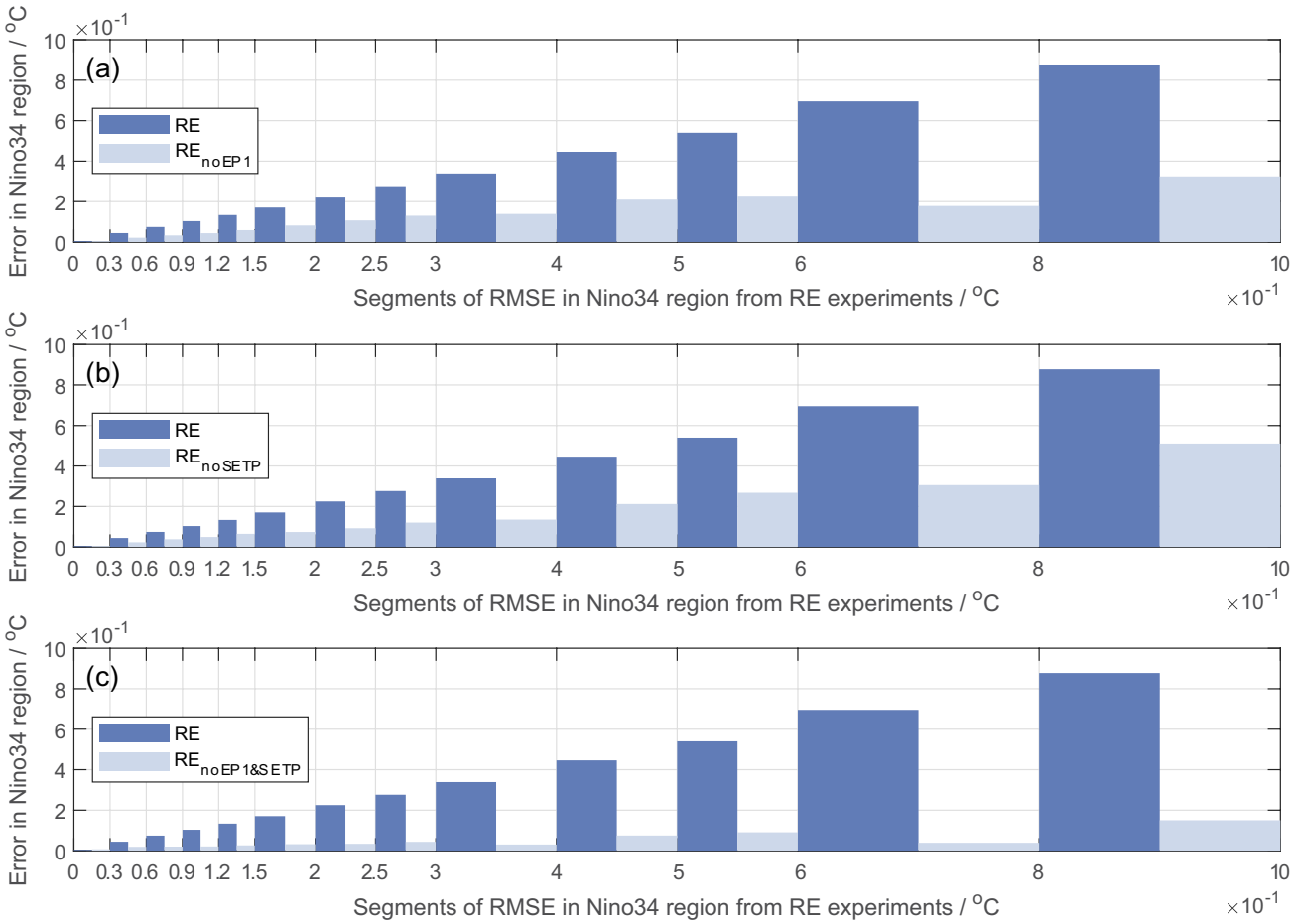

Fig. 6 Prediction errors in the Niño34 regions from RE, RE_{noEP1}, RE_{noSETP} and $RE_{noEP1\&noSETP}$ experiments. The horizontal axis represents the interval division of the final prediction errors of the 1000 sets of prediction experiments in the RE experiment. The vertical axis denotes the average prediction errors under the corresponding observational error conditions (light blue bars) and the intensified observation experiment (dark blue bars)

experiment is adopted, the prediction errors are smaller than those in the RE experiment. Especially for the $RE_{noEP1\&SETP}$ experiment, the prediction errors in the Niño3.4 region are all reduced to less than 0.1 °C. Besides, the larger the prediction errors in the RE experiment, the more obvious the improvement of the $RE_{noEP1\&SETP}$ experiment on the La Niña prediction. Here, we introduce an index to quantify the effect of "observations" in those sensitive regions on the improvement of the La Niña prediction, called benefit rate (BR) which is written as $R = \frac{E-E_{TA}}{E}$. E denotes the prediction error in the RE experiment, and E_{TA} denotes the prediction error in the experiment of target observation in the TA region. As shown in Fig. 7, regardless of the target month, conducting the target observation experiment can always enhance the La Niña prediction skill. Moreover, this improvement is most significant for the SST prediction in the Niño3.4 region, with the BR generally reaching over 60% (up to 80%). However, when the prediction skill in the RE experiment is high and the prediction error is very small, an abnormal phenomenon that the prediction skill deteriorates may occur for the target observation. For example, in the first column of Fig. 7a and the second column of Fig. 7b, intensifying observations in the CNOP-identified sensitive regions tends to promote error growth. This situation is relatively easy to understand. When the original prediction skill is high, it implies that the error growth caused by the initial error has a positive–negative cancellation effect. When only the initial error in a certain region is reduced, this balance is disrupted. Consequently, the prediction error will grow rapidly in a certain direction, resulting in this abnormal phenomenon.

To further verify the importance of the initial condition in the equatorial eastern Pacific and the tropical southeastern Pacific compared to other regions, we additionally add four groups of observation experiments. That is, we randomly select four regions (termed as RA01, RA02, RA03 and RA04) of comparable volume and remove the initial errors in these regions (see Table 3). Then, we repeat the prediction experiments and compare their results with those

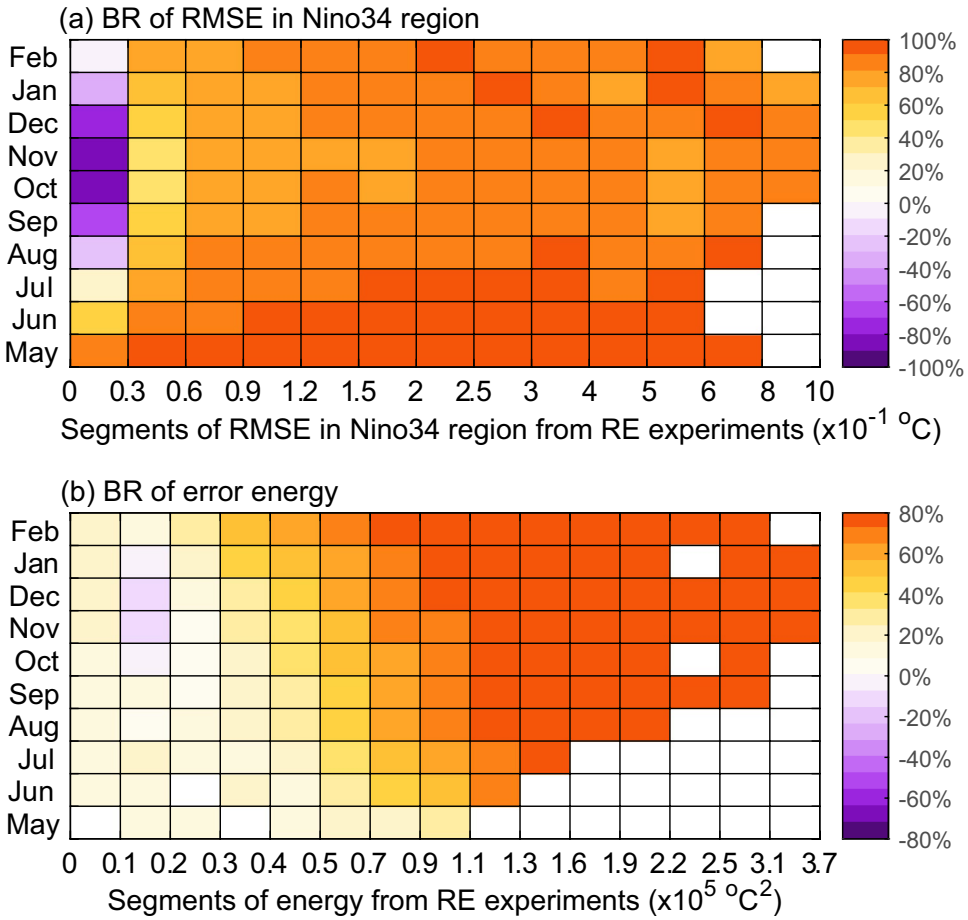

Fig. 7 Benefit rates of the $RE_{noEP1\&SETP}$ experiment as a function of target month and prediction error in the corresponding RE experiment. BR in **a** is obtained using the prediction error in the Niño3.4 region. BR in **b** is obtained using the error energy of the whole tropical Pacific

of the target observation experiment revealed by the OIEs. Results are shown in Fig. 8. It can be seen that the prediction returns of all observation experiments are lower than those of the $RE_{noEP1\&SETP}$ experiment. Only the improvement in the prediction skill of intensifying observations in the RA03 region is close to that of the $RE_{noEP1\&SETP}$ experiment, while the effects of others are far weaker than the latter. This is because the RA03 region covers most of the areas identified by CNOP.

Evidently, the former results fully demonstrate that the sensitive regions revealed by OIEs can serve as key areas for targeted observations. This study can provide theoretical guidance for further improving the prediction level of the La Niña event.

5 Conclusions and discussions

In the current era of rapid AI development, numerous purely data-driven ENSO models with high predictive skills are developed. However, the extent to which these models rely on the initial input fields has not been deeply explored. If data-driven models can learn the nonlinear characteristics of dynamical systems, they will inevitably exhibit a similar "butterfly effect" as dynamical models. Therefore, it is crucial to investigate which types of initial errors cause the greatest error growth in ENSO predictions. Here, with the CNOP approach, we adopt the data-driven model developed by Zhou and Zhang (2023) to explore the potential impact of the error in the input fields on the La Niña predictions during 2020–2022. The core and significance of the present study are shown in Fig. 9.

To apply the CNOP approach to the data-driven model, we designed an iterative optimization algorithm based on large samples to solve the CNOP without adjoint model. This groundbreaking strategy not only simplifies the computational process but also enhances the scalability and applicability of the CNOP method across diverse modeling frameworks. This novel methodology offers a robust and adaptable solution for addressing complex predictability challenges in climate science.

Based on the ensemble-based CNOP approach, two types of OIEs are obtained: one processes positive value (POIE) in the eastern tropical Pacific while the other has similar pattern but with negative value (NOIE). These OIEs exhibit spatial structures similar to the Bjerknes mode, leading to rapid error growth through strong positive feedback mechanisms. The POIEs and NOIEs cause contrasting prediction

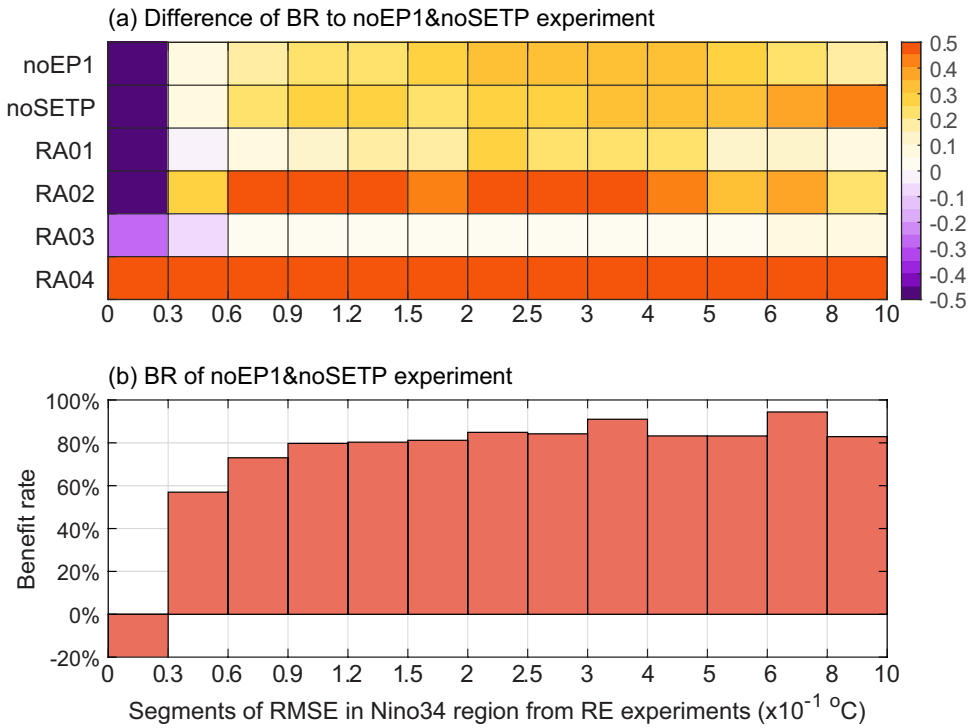

Fig. 8 **a** the difference of BRs to the noEP1&noSETP experiment and **b** mean BR in the noEP1&noSETP experiment

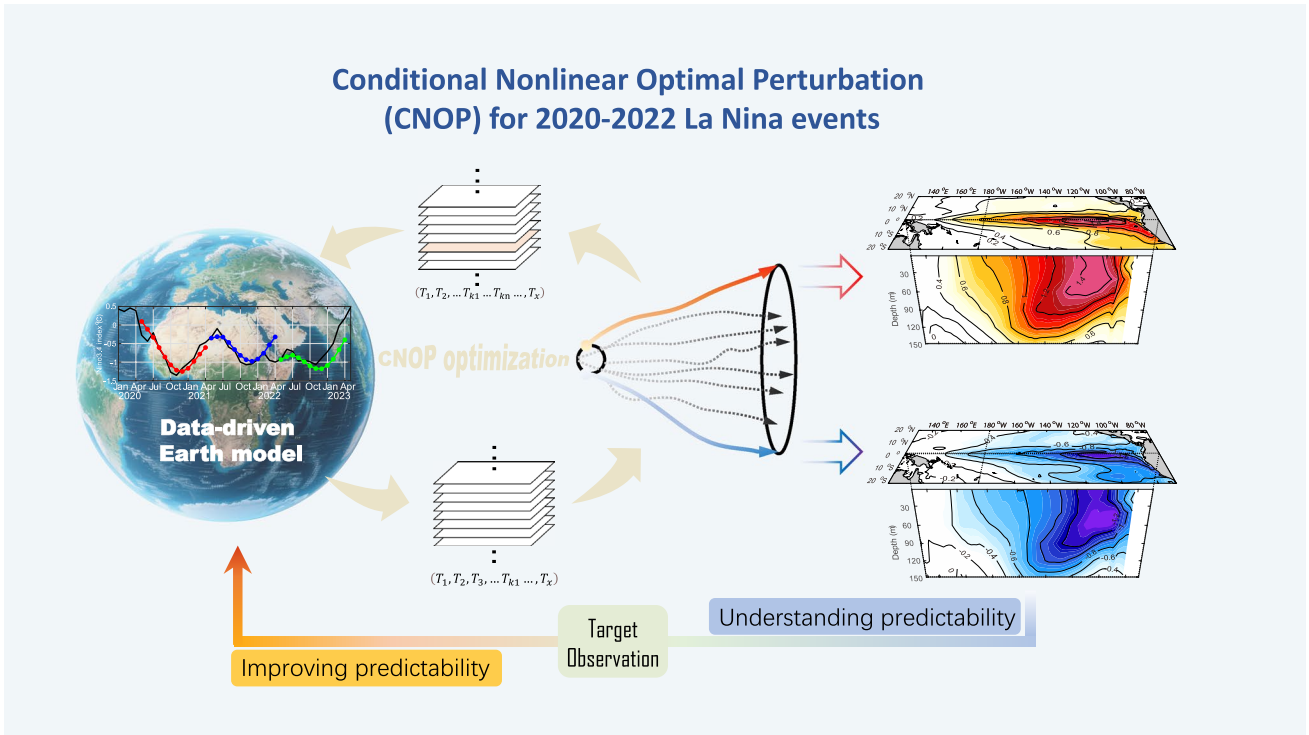

Fig. 9 Integrating an CNOP analysis with a data-driven transformer model to study and improving the predictability of 2020–2022 La Niña events

error evolutions, with POIEs resembling El Niño development, while NOIEs resemble La Niña development. These errors grow quickly due to the triggered Bjerknes positive feedback, thus generating the "butterfly effect". Notably, the 2021 La Niña prediction is particularly sensitive to initial conditions compared to the 2020 and 2022 events. This heightened sensitivity indicates that the 2021 La Niña event has the lowest predictability. Besides, the error growth rates induced by POIEs are significantly larger than those caused by NOIEs, suggesting that initial temperature errors

with positive values are more likely to lead to substantial prediction discrepancies. The triggered Bjernkes feedback accounts for this difference in sensitivity or predictability. In particular, the induced stronger HC-SST feedbacks for 2021 La Niña and POIE tend to make initial temperature errors in the subsurface layer more likely to influence the surface layer, leading to more significant increases in prediction errors.

Although this study only examined the theoretical aspect of the sensitivity to initial errors from a data perspective, it also provides application value for target observation and optimizing data-driven models to improve the prediction of La Niña. For example, the study emphasizes that the ocean temperature error in the upper 150 m of the equatorial eastern Pacific is an important source of the maximum prediction error, which means that high-resolution measurements in these areas can help reduce initial errors and improve the accuracy of the La Niña prediction (the theoretical improvement effect can reach over 80%). At the same time, in terms of model training, the accuracy of sea temperature in the central and eastern Pacific should also be emphasized to avoid introducing large errors in the "black box". Of course, when it is truly implemented in applications, there will be many more considerations, and this study alone is far from sufficient. Besides, whether the results are universal still needs to be continuously verified in future work. Nevertheless, we believe the result of the present study is universal. When compared with previous studies based on dynamic models, whether they are complex or simple, the patterns of the OIE that can cause the largest error growth in ENSO forecasts are basically the same (Duan and Hu 2016; Duan et al. 2018; Hou et al. 2019). They are mainly located in the equatorial eastern Pacific and the tropical southeastern Pacific. On one hand, it implies that the data-driven model can capture the dynamic characteristics of ENSO predictability. On the other hand, it also reflects that the sensitive areas are inherent properties of ENSO prediction and do not exhibit model dependence. Conducting intensive observations in the sensitive areas identified by CNOP can not only enhance the prediction skills of dynamic models but also improve the performance of AI models.

Acknowledgements We express our gratitude to all reviewers for their valuable suggestions during the preparation of this work.

Funding National Natural Science Foundation of China (42405062, 42030410), Ministry of Science and Technology of the People's Republic of China (2020YFA0608802), Jiangsu Innovation Research Group (JSSCTD 202346).

Data availability The model data are produced by the Climate Model Intercomparison Project Phase 6 (CMIP6) (downloaded from https://aims2.llnl.gov/search/cmip6/). The reanalysis data of ocean temperature and wind stress are from the NCEP Global Data Assimilation System (GODAS) is available via Behringer et al. (1998) (downloaded from https://www.psl.noaa.gov/data/gridded/data.godas.html).

Code availability Scripts and software used for the analysis in the study are available from the first or corresponding author upon reasonable request.

Declarations

Competing interests The authors have no competing interests to declare.

Ethical approval and consent to participate The authors confirm that this article is original research and has not been published previously in any journal.

Consent for publication The authors have agreed to submit this manuscript in its current form for publication in the journal.

References

Alexander MA, Blade I, Newman M, Lanzante JR, Lau NC, Scott JD (2002) The atmospheric bridge: the influence of ENSO teleconnections on air-sea interaction over the global oceans. J Climate 15(16):2205–2231

Behringer DW, Ji M, Leetmaa A (1998) An improved coupled model for ENSO prediction and implications for ocean initialization. Part I: the ocean data assimilation system. Mon Weather Rev 126(4):1013–1021

Chen DK, Zebiak SE, Cane MA, Busalacchi AJ (1997) Initialization and predictability of a coupled ENSO forecast model. Mon Weather Rev 125(5):773–788

Dong X, Zhang RH, Chuan Gao JH, Chen M (2025) Thermodynamic processes prolong La Niña events in a hybrid coupled ocean-atmosphere model. Clim Dyn. https://doi.org/10.1007/s00382-024-07564-w

Duan WS, Hu JY (2016) The initial errors that induce a significant "spring predictability barrier" for El Niño events and their implications for target observation: results from an earth system model. Clim Dyn 46(11–12):3599–3615. https://doi.org/10.1007/s00382-015-2789-5

Duan WS, Li XQ, Tian B (2018) Towards optimal observational array for dealing with challenges of El Niño-Southern Oscillation predictions due to diversities of El Niño. Clim Dyn 51(9–10):3351–3368. https://doi.org/10.1007/s00382-018-4082-x

Duan WS, Mu M (2018) Predictability of El Niño-Southern oscillation events. Oxf Res Encycl Clim Sci. https://doi.org/10.1093/acrefore/9780190228620.013.80

Feng J, Lian T, Ying J, Li JD, Li G (2020) Do CMIP5 models show El Niño diversity? J Climate 33(5):1619–1641. https://doi.org/10.1175/Jcli-D-18-0854.1

Freund MB, Brown JR, Henley BJ, Karoly DJ, Brown JN (2020) Warming patterns affect El Niño diversity in CMIP5 and CMIP6 models. J Climate 33(19):8237–8260. https://doi.org/10.1175/Jcli-D-19-0890.1

Gao C, Chen M, Zhou Lu, Feng L, Zhang RH (2022) The 2020–2021 prolonged La Niña evolution in the tropical Pacific. Sci China Earth Sci 65(12):2248–2266. https://doi.org/10.1007/s11430-022-9985-4

Gao C, Zhou L, Zhang RH (2023) A transformer-based deep learning model for successful predictions of the 2021 second-year La Niña condition. Geophys Res Lett 50(12). https://doi.org/10.1029/2023GL104034.

Geng T, Jia F, Cai WJ, Wu LX, Gan BL, Jing Z, Li SJ, McPhaden MJ (2023) Increased occurrences of consecutive La Niña events

under global warming. Nature 619(7971):774. https://doi.org/10.1038/s41586-023-06236-9

Ham YG, Kim JH, Luo JJ (2019) Deep learning for multi-year ENSO forecasts. Nature 573(7775):568. https://doi.org/10.1038/s41586-019-1559-7

Ham YG, Kim JH, Kim ES, On KW (2021) Unified deep learning model for El Niño/Southern Oscillation forecasts by incorporating seasonality in climate data. Sci Bull 66(13):1358–1366. https://doi.org/10.1016/j.scib.2021.03.009

Hou MY, Duan WS, Zhi XF (2019) Season-dependent predictability barrier for two types of El Niño revealed by an approach to data analysis for predictability. Clim Dyn 53(9–10):5561–5581. https://doi.org/10.1007/s00382-019-04888-w

Ibebuchi CC, Richman MB (2024) Deep learning with autoencoders and LSTM for ENSO forecasting. Clim Dyn 62(6):5683–5697. https://doi.org/10.1007/s00382-024-07180-8

Jin EK et al (2008) Current status of ENSO prediction skill in coupled ocean-atmosphere models. Clim Dyn 31(6):647–664. https://doi.org/10.1007/s00382-008-0397-3

Li T, Tang YM, Lian T, Hu AF (2024) Quantifying the relative contributions of the Global Oceans to ENSO predictability with deep learning. Geophys Res Lett. https://doi.org/10.1029/2023GL106584

Liu T, Song XS, Tang YM (2022) The predictability study of the two flavors of ENSO in the CESM model from 1881 to 2017. Clim Dyn 59(11–12):3343–3358. https://doi.org/10.1007/s00382-022-06269-2

Liu T, Gao YQ, Song XS, Gao C, Tao LJ, Tang YM, Duan WS, Zhang RH, Chen DK (2023) A multi-model prediction system for ENSO. Sci China Earth Sci 66(6):1231–1240. https://doi.org/10.1007/s11430-022-1094-0

Lou JL, Newman M, Hoell A (2023) Multi-decadal variation of ENSO forecast skill since the late 1800s. NPJ Clim Atmos Sci. https://doi.org/10.1038/s41612-023-00417-z

Mu M, Duan WS, Wang B (2003) Conditional nonlinear optimal perturbation and its applications. Nonlinear Process Geophys 10(6):493–501

Mu B, Qin B, Yuan SJ (2021) ENSO-ASC 1.0.0: ENSO deep learning forecast model with a multivariate air-sea coupler. Geosci Model Dev 14(11):6977–6999. https://doi.org/10.5194/gmd-14-6977-2021

Mu B, Qin B, Yuan SJ (2022) ENSO-GTC: ENSO deep learning forecast model with a global spatial-temporal teleconnection coupler. J Adv Model Earth Sy 14(12). https://doi.org/10.1002/qj.4882

Philander SGH (1983) El-Niño Southern Oscillation phenomena. Nature 302(5906):295–301. https://doi.org/10.1038/302295a0

Planton et al (2021) Evaluating Climate Models with the CLIVAR 2020 ENSO Metrics Package. Bull Amer Meteor Soc 102:E193–E217. https://doi.org/10.1175/BAMS-D-19-0337.1

Qi QQ, Duan WS, Xu H (2021) The most sensitive initial error modes modulating intensities of CP- and EP- El Niño events. Dyn Atmos Oceans. https://doi.org/10.1016/j.dynatmoce.2021.101257

Qin B, Yang ZY, Mu M, Wei YT, Cui YH, Fang XH, Dai GK, Yuan SJ (2024) The first kind of predictability problem of El Niño predictions in a multivariate coupled data-driven model. Q J R Meteorol Soc 150(765):5452–5471. https://doi.org/10.1002/qj.4882

Rao WX, Tang YM, Wu YL, Shen ZQ, Song XZ, Li XJ, Lian T, Chen DK, Zhou F (2023) A new ensemble-based targeted observational method and its application in the TPOS 2020. Natl Sci Rev. https://doi.org/10.1093/nsr/nwad231

Tan XX, Tang YM, Lian T, Zhang SW, Liu T, Chen DK (2020) Effects of semistochastic westerly wind bursts on ENSO predictability. Geophys Res Lett. https://doi.org/10.1029/2019GL086828

Tang YM et al (2018) Progress in ENSO prediction and predictability study. Natl Sci Rev 5(6):826–839. https://doi.org/10.1093/nsr/nwy105

Tao LJ, Duan WS, Vannitsem S (2020) Improving the forecasts of El Niño diversity: a nonlinear forcing singular vector approach. Clim Dyn 55:739–754. https://doi.org/10.1007/s00382-020-05292-5

Tao LJ, Duan WS, Jiang L (2022) Model errors of an intermediate model and their effects on realistic predictions of El Niño diversity. Int J Climatol. https://doi.org/10.1002/joc.7656

Timmermann A et al (2018) El Niño-Southern Oscillation complexity. Nature 559(7715):535–545. https://doi.org/10.1038/s41586-018-0252-6

Wang TY, Huang P, Yang XK (2024) Understanding the low predictability of the 2015/16 El Niño event based on a deep learning model. Adv Atmos Sci 41(7):1313–1325. https://doi.org/10.1007/s00376-024-3238-3

Yeh SW, Kug JS, Dewitte B, Kwon MH, Kirtman BP, Jin FF (2009) El Niño in a changing climate. Nature 461(7263):511-U570. https://doi.org/10.1038/nature08316

Yu JY, Fang SW (2018) The distinct contributions of the seasonal footprinting and charged-discharged mechanisms to ENSO complexity. Geophys Res Lett 45(13):6611–6618. https://doi.org/10.1029/2018gl077664

Yu YS, Duan WS, Xu H, Mu M (2009) Dynamics of nonlinear error growth and season-dependent predictability of El Niño events in the Zebiak-Cane model. Q J R Meteorol Soc 135(645):2146–2160. https://doi.org/10.1002/qj.526

Zhang RH et al (2020) A review of progress in coupled ocean-atmosphere model developments for ENSO studies in China. J Oceanol Limnol 38(4):930–961. https://doi.org/10.1007/s00343-020-0157-8

Zhang RH, Gao C, Feng LC (2022) Recent ENSO evolution and its real-time prediction challenges. Natl Sci Rev. https://doi.org/10.1093/nsr/nwac052

Zhang RH, Zhou L, Gao C, Tao LJ (2024a) Real-time predictions of the 2023–2024 climate conditions in the tropical Pacific using a purely data-driven Transformer model. Sci China Earth Sci 67(12):3709–3726. https://doi.org/10.1007/s11430-024-1396-x

Zhang RH, Zhou L, Gao C, Tao LJ (2024b) A transformer-based coupled ocean-atmosphere model for ENSO studies. Sci Bull 69(15):2323–2327. https://doi.org/10.1016/j.scib.2024.04.048

Zheng YC, Duan WS, Tao LJ, Ma JJ (2023) Using an ensemble nonlinear forcing singular vector data assimilation approach to address the ENSO forecast uncertainties caused by the "spring predictability barrier" and El Niño diversity. Clim Dyn 61(11–12):4971–4989. https://doi.org/10.1007/s00382-023-06834-3

Zhou L, Zhang RH (2023) A self-attention-based neural network for three-dimensional multivariate modeling and its skillful ENSO predictions. Sci Adv 9(10):eadf2827. https://doi.org/10.1126/sciadv.adf2827.

Zhou L, Zhang RH (2022) A hybrid neural network model for ENSO prediction in combination with principal oscillation pattern analyses. Adv Atmos Sci 39(6):889–902. https://doi.org/10.1007/s00376-021-1368-4

Zhou L, Zhang RH (2024) ENSO-related precursor pathways of interannual thermal anomalies identified using a transformer-based deep learning model in the tropical Pacific. Geophys Res Lett 51:e2023GL107347. https://doi.org/10.1029/2023GL107347